Four-Winding Integrated Inductor Transformer Structure for Dual Active Bridge Converter

Siddhesh Shinde, *Graduate Student Member, IEEE*, Gautam Rituraj, *Member, IEEE*, Gautham Ram Chandra Mouli, *Senior Member, IEEE*, Vishnu Mahadeva Iyer, *Senior Member, IEEE*, and Pavol Bauer, *Senior Member, IEEE*

***Abstract*—In a dual active bridge converter, the split series inductance configuration with finite magnetizing inductance can provide an additional degree of freedom to optimize the converter's performance. However, this magnetic configuration results in three separate magnetic structures, which increases the volume and footprint. To address this issue, this article proposes a four-winding integrated magnetic structure comprising decoupled primary inductance, secondary inductance, and a transformer capable of independent tuning. The fluxes produced by primary and secondary inductors within the integrated structure consistently oppose in the middle leg of the inductor core, resulting in reduced losses and a smaller volume. A design methodology based on an analytical model has also been developed to systematize the design process. A sensitivity analysis is performed using the finite element method to verify the decoupling operation. An 11 kW, 775 V/450 V prototype is implemented, and the integrated magnetic structure is compared with its discrete implementation under steady-state thermal conditions at different ambient temperatures. A volume reduction of 12.1% and magnetic loss reduction of 4.5% is achieved, while the converter efficiency remains higher or comparable to that of the discrete implementation across the entire operating range.**

***Index Terms*—Dual active bridge (DAB), integrated inductor transformer, integrated magnetics, reluctance modeling, split inductor.**

I. Introduction

With the growing trend towards transportation electrification, power converters are expected to be compact, efficient, and cost-effective [1]. The size and weight of power converters are largely governed by magnetics, making them a critical bottleneck in achieving high efficiency and power density [2]. This has necessitated advancements in magnetic design, such as integrating inductor and transformer functionalities within a single magnetic structure, thereby facilitating miniaturization. The integrated magnetic structures often do not provide greater design flexibility due to the magnetic coupling and interdependent nature of their inductances. This lack of flexibility can result in suboptimal design and operation of power converters.

The Dual Active Bridge (DAB) converter is one of the standard topologies used in the dc-dc stage of an Electric Vehicle (EV) charger [1]. The series inductor controls the power transfer between the input and output full bridges in the DAB converter. Splitting the series inductor between the primary and secondary sides of the transformer influences the impedance seen by both the full-bridges. These split inductances, together with the magnetizing inductance, affect the key performance characteristics of the DAB power converter, such as RMS current, peak current, and zero voltage switching (ZVS) range [3], [4]. Furthermore, the magnetizing current in the split inductance configuration is supplied by both the bridges [5], directly influencing the core loss characteristics of the transformer. Therefore, an integrated magnetic structure with a split inductor configuration for the DAB converter can provide greater design flexibility if the individual series inductances can be tuned without affecting the magnetizing inductance. In the literature, several integrated magnetic structures have been proposed that allow integration of series inductance along with transformer functionality. These methods can be broadly classified into two categories: Method–1: Utilizing the leakage inductance as series inductance [6], [7], [8], [9], [10], [11], [12], [13], [14], [15], [16], [17], [18]; and Method–2: Separate transformer and inductor windings wound on the same core structure [19], [20], [21], [22], [23], [24].

In the first method, leakage inductance is created by reducing transformer winding coupling or by providing a separate leakage flux path within the core. In [6], [7], [8], the leakage inductor is created by spacing primary and secondary windings. In this method, an accurate distance is required between the windings to store the leakage energy; the value of inductance is limited due to inter-winding spacing constraints. Similarly, [9] achieves the required leakage inductance using PCB windings on a three-leg core, integrating three transformers and an ac inductor to reduce component count and losses. In [10], the transformer's primary and secondary windings were put in sections to introduce leakage flux in air. In this sectional winding method, it is demonstrated that the winding losses increase with a higher leakage inductance value. In [11], a leakage layer made of high-permeability material was used between the primary

Received 18 August 2025; revised 13 November 2025; accepted 11 December 2025. Date of publication 22 December 2025; date of current version 20 March 2026. Recommended for publication by Associate Editor J. Biela. *(Corresponding author: Siddhesh Shinde.)*

Siddhesh Shinde, Gautam Rituraj, Gautham Ram Chandra Mouli, and Pavol Bauer are with the Department of Electrical Sustainable Energy, Delft University of Technology, 2628 CD Delft, The Netherlands (e-mail: s.s.shinde-1@tudelft.nl; g.rituraj@tudelft.nl; g.r.chandramouli@tudelft.nl; p.bauer@tudelft.nl).

Vishnu Mahadeva Iyer is with the Department of Electrical Engineering, Indian Institute of Science, Bengaluru 560012, India (e-mail: vishnumi@iisc.ac.in).

Color versions of one or more figures in this article are available at https://doi.org/10.1109/TPEL.2025.3646768.

Digital Object Identifier 10.1109/TPEL.2025.3646768

and secondary windings. The thickness and position of the layer are adjusted to obtain the desired leakage inductance. However, this high-permeability material can lead to insulation breakdown and poses difficulty in construction. In [8], [12], and [13], primary and secondary were separately wound on the outer legs of the transformer core, and the middle leg with the air gap was used as a leakage flux path. Similarly, in [14], the thickness and relative permeability of a magnetic shunt located between the primary and secondary windings were used to tune the leakage inductance. Both air gaps in the middle leg and shunt methods allow for the accurate tuning of the leakage inductance. However, integrating large values of leakage inductance reduces both the magnetizing inductance and the coupling between the transformer's windings. To overcome the reduction in magnetizing inductance and improve transformer coupling, [15] proposed the core structure, which has primary and secondary asymmetric windings on both the outer legs of the transformer. The middle leg with the air gap carries the leakage flux. However, this method has a complex winding arrangement, which produces higher losses than the discrete structure due to increased ac winding resistance. A similar magnetic integration method using an asymmetric winding was employed in [16] for a three-phase LLC converter, which integrates the functionality of six inductors and six transformers, taking advantage of flux cancellation. In [17], the authors presented a split-UI core integrated structure for a dual-transformer DAB converter, which adopts a design concept similar to the asymmetric winding integration approach. This configuration effectively reduces ac winding losses by leveraging the split-core structure. Furthermore, in [18], the authors integrated an inductor, transformer, and leakage inductor into a single magnetic structure for a current-fed DAB converter, using an approach similar to asymmetric winding integration. A comparison between the asymmetric winding magnetic integration method with separated outer legs and the sectional winding method is presented in [10]. It is observed that for higher values of series inductance, the asymmetric method proves more beneficial than the sectional method. However, in the asymmetric winding integration method, introducing an air gap in the outer leg to control magnetizing inductance can reduce leakage inductance due to the shared magnetic reluctance path.

In the second magnetic integration method, separate inductors and transformer windings are wound on a single core structure. Fluxes produced by these windings share and utilize the same core. In [19], inductor windings are wound on both the outer legs, and transformer primary and secondary windings are wound on the middle; there are no gaps in the core. This design creates a series inductance on the primary side and is controlled by the number of turns. In this design, there is limited energy storage and a risk of core saturation due to the absence of an air gap. In addition, it showcases the conditional coupling between the inductor and transformer flux. In [20], a similar method was proposed with the air gap in both the outer legs; in this case, leakage flux path flows exclusively through the outer legs and cancels out in the middle leg, providing better decoupling. However, the air gap introduced in the mutual flux path reduced magnetizing inductance. In [21], a custom matrix core structure was used, and the secondary side winding was physically extended around the gapped core leg to create the series inductor on the secondary side. This design decouples the inductor and transformer fluxes, but showcases the current distribution problem and poor space utilization of the inductor core leg. Similarly, in [22], the primary winding is extended around a gapped leg to create the inductor on the primary side of the matrix transformer; however, this structure features a complex PCB winding with a fractional turn connection for current sharing. In [23], an integrated magnetic structure was proposed for a DAB converter, which consisted of two I-cores with air gaps connected to the UU-core on the side. The inductor windings are wound on both I-cores, and transformer windings on the UU core. This structure creates a split inductor, but the decoupling of the transformer and inductor flux is achieved if both the split inductors produce the same magnitude of flux, and therefore, the primary and secondary side inductors cannot be tuned independently. Additionally, this design requires precise alignment of I cores, and it utilizes two different core materials, resulting in a complex design. In [24], both primary and secondary transformer windings were wound around the inductor leg, which was separated from the transformer leg by the distributed air gap. This design results in a series inductor on both primary and secondary sides, but the inductor fluxes are coupled due to the overlapping of their respective windings.

From the abovementioned literature survey, it has been found that with the first method [6], [7], [8], [9], [10], [11], [12], [13], [14], [15], [16], [17], [18], the leakage inductance (L_e) appears on both the primary and secondary sides, but cannot be tuned independently. Additionally, in [6], [7], [8], [9], [10], [11], [12], [13], [14], the introduction of L_e reduces magnetizing inductance (L_m) and transformer coupling. Even though the asymmetric windings integration method [10], [15], [16], [17], [18] shows no reduction in L_m, the control of L_m by introducing an air gap in the outer leg affects L_e as they are coupled. In the second integration method, the integrated series inductor (L) entirely appears on either side of the transformer [19], [20], [21], [22]. In case if series inductance is split between primary inductance (L_1) and secondary inductance (L_2) [23], [24], it is not possible to independently tune them due to flux coupling between the inductor flux (ϕ_{ind}) and transformer flux (ϕ_{tx}). In this context, this work proposes a 4-Winding Integrated Inductor Transformer (4W-ILX) structure for the DAB converter, which has the following key contributions, compared to the state-of-the-art integrated magnetic designs, as presented in Table I.

1) The proposed 4W-ILX magnetic structure allows integration and independent tuning of the L_1, L_2, and L_m. The design guarantees weak coupling between L_1 and L_2 inductor fluxes and ϕ_{tx}. In addition, the coupling between the transformer winding always remains high.
2) The proposed 4W-ILX magnetic structure reduces volume and total losses while maintaining (or improving) converter efficiency in a wide operating range compared to the discrete split inductance and transformer structure.
3) The design methodology for 4W-ILX is also developed using an analytical model derived from the simplified

TABLE I
COMPARISON OF ILX STRUCTURE AGAINST OTHER STATE-OF-THE-ART

	Literature	Transformer coupling	Reduction in L_m	L_e, L or L_1, L_2 control method	Flux coupling ϕ_{ind} and ϕ_{tx}	Independent tuning of L_1, L_2	Compared to discrete	DC-DC Converter
Method 1	Ortiz et al. [6]	L_e dependent	Yes	Winding space	NA	No	NA	DAB
	Pavlovsky et al. [11]	L_e dependent	Yes	Leakage layer	NA	No	NA	Resonant
	Biela et al. [12]	L_e dependent	Yes	Air-gap	NA	No	NA	Resonant
	Zhang et al. [14]	L_e dependent	Yes	Shunt tuning	NA	No	NA	LLC
	Li et al. [15]	High	No	Middle limb air gap	NA	No	3.7% ↓ volume with 8% ↑ losses	CLLC
Method 2	Kim et al. [19]	High	No	Outer turns	Partially	L_1 only	NA	PSFB
	Liu et al. [21]	High	No	Turns and air gap	Weakly	L_2 only	NA	CLL
	Ahmed et al. [22]	High	No	Turns and air gap	Weakly	L_1 only	0.6% ↑ efficiency	LLC
	Cao et al. [23]	High	No	Turns and air gap	Conditional	No	12.1% ↓ volume	DAB
	Yang et al. [24]	High	No	Turns and air gap	Partially	No	NA	CLLC
	This work	**High**	**No**	**Turns and air gap**	**Weakly**	$\boldsymbol{L_1}$ **and** $\boldsymbol{L_2}$	**12.1% ↓ volume with 4.5% ↓ losses**	**DAB**

Note: The designs compared in Table I are intended for different applications, each with distinct voltage, power (kVA), and frequency specifications.

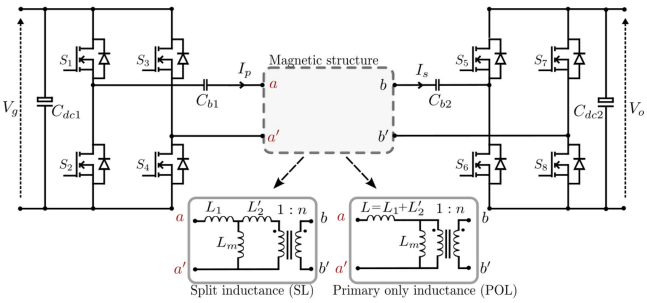

Fig. 1. DAB converter with SL and POL magnetic configuration.

reluctance representation. This model is used to determine the number of turns and air-gap length required to achieve the desired value of L_1 and L_2. The proposed design is subsequently validated through Finite Element Method (FEM) simulations.

The rest of this article is organized as follows. Section II describes the system overview and problem formulation. Section III explains the construction and flux distribution of the 4W-ILX structure. Section IV presents the analytical model based on reluctance. Section V shows the design methodology and sensitivity analysis using FEM. Section VI presents the developed experimental setup, and measured electrical parameters of 4W-ILX and the discrete structure as well as their performance under identical thermal conditions and operating points. Finally, Section VII concludes this article.

II. SYSTEM DESCRIPTION AND PROBLEM FORMULATION

This section analyzes the effect of split inductance (SL) and primary only inductance (POL) magnetic configurations on the DAB converter's performance. In Fig. 1, switches S_1 to S_8 generate phase-shifted excitation voltages for the selected magnetic configuration. C_{dc1} are C_{dc2} are dc-bus capacitors, whereas C_{b1} and C_{b2} are dc-blocking capacitors. V_g and V_o are the input and the output voltages, respectively. In the SL configuration, L_1 is the primary side inductance, L_2' is the secondary side inductance referred to the primary, and L_m is the magnetizing inductance. Whereas, in the POL configuration, L is the primary side inductance with a value equivalent to $L_1 + L_2'$, and the transformer turns ratio is given by n. Due to the finite value of L_m, the primary side current I_p and secondary side current I_s are functions of inductor ratios γ and β, respectively, as defined as follows:

$$\gamma = \frac{L_m}{L_1 + L_2'} \quad \text{and,} \quad \beta = \frac{L_2'}{L_1}. \tag{1}$$

For the POL configuration, $L_1 + L_2'$ is substituted as L in γ, and β is zero. Moreover, during switching instants $\frac{DT_s}{2}$ and $\frac{T_s}{2}$, the primary side current I_{1p} and I_{2p} and secondary side current I_{1s} and I_{2s}, respectively, can be calculated using (2)–(5) as follows:

$$I_{1p} = K\left[\frac{\gamma(1+\beta)[2D+(M-1)]+\beta(2D-1)}{\gamma(1+\beta)^2+\beta}\right] \tag{2}$$

$$I_{2p} = K\left[\frac{\gamma(1+\beta)+\beta+M\gamma(1+\beta)(2D-1)}{\gamma(1+\beta)^2+\beta}\right] \tag{3}$$

$$I_{1s} = \frac{K}{n}\left[\frac{\gamma(1+\beta)(2D-1)+M[\gamma(1+\beta)+1]}{\gamma(1+\beta)^2+\beta}\right] \tag{4}$$

$$I_{2s} = \frac{K}{n}\left[\frac{M[\gamma(1+\beta)+1](2D-1)+\gamma(1+\beta)}{\gamma(1+\beta)^2+\beta}\right]. \tag{5}$$

In (2)–(5), M is (V_o/nV_g), representing the voltage ratio, T_s is the switching cycle time, and D is the duty ratio. Here, D denotes the phase shift between the primary and secondary side full bridges (Φ) and can be expressed as $\frac{\Phi}{T_s/2}$. For SL and POL configurations, the constant K is equal to $\frac{T_s V_g}{4L_1}$ and $\frac{T_s V_g}{4L}$, respectively. The peak current and RMS current of the primary and secondary sides of the DAB transformer are derived using (2)–(5).

Fig. 2 shows the comparison of normalized RMS and peak current of DAB converter with SL and POL configurations for γ of 15 and unity turns ratio. I_{base} is the ratio of the DAB

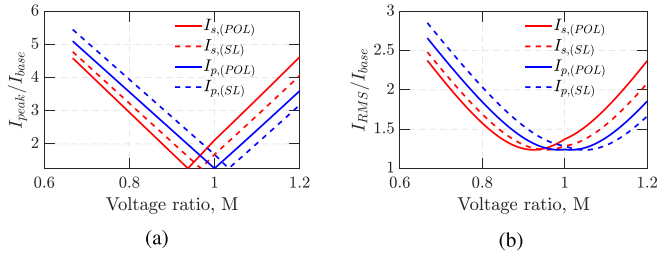

Fig. 2. Comparison between SL configuration ($\beta = 1$) and POL configurations for $\gamma = 15$ and $n = 1$. (a) Normalized peak current. (b) Normalized RMS current.

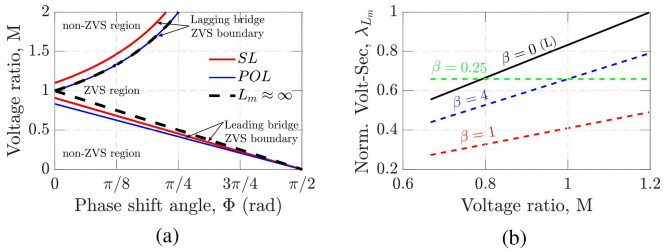

Fig. 3. (a) ZVS boundaries of leading and lagging bridges for both SL ($\beta = 1$) and POL configuration $\gamma = 5$. (b) Normalized volt-seconds across magnetization inductor for different values of β at $\Phi = \pi/2$.

converter's rated output power P_o to the maximum output voltage V_{o-max} and is used to normalize the current values. It is observed that the SL configuration results in lower peak current and RMS current values for high voltage ratios M for both the primary and secondary sides, indicating lower current stress and lower conduction losses for the high voltage operating region. Whereas, for lower values of M, the peak and RMS current values are higher in both the primary and secondary sides for the SL configuration compared to the POL configuration. This difference in the peak and RMS current between the two magnetic configurations increases with lower values of γ.

SL configuration also influences the ZVS boundary and volt-seconds applied across the magnetizing inductance, as shown in Fig. 3. ZVS boundaries for both SL and POL configurations are compared in Fig. 3(a) for γ of 5, and for the SL configuration, particularly β of unity. Finite magnetizing inductance influences the ZVS boundaries of full bridges. For the POL configuration, only the ZVS boundary of the leading bridge is extended, and for the SL configuration, the ZVS boundaries of both the leading and lagging bridges are extended. The ZVS boundary conditions for L_m close to infinity are shown for reference. The reduction in γ leads to a greater extension of the ZVS boundaries in both configurations.

The volt-seconds across the magnetizing inductance dictate the maximum flux density and therefore influence the core losses. Fig. 3(b) shows the normalized volt-seconds applied during the positive half cycle across magnetizing inductance λ_{L_m} for different values of β. The normalized λ_{L_m} value of unity indicates the volt-seconds at maximum output voltage V_{o-max}. It is observed that for the POL configuration where β is zero, the output voltage V_o dictates the volt-seconds across the magnetizing inductance and therefore reaches unity for a high value of M. Whereas, for the SL configuration, the volt-seconds across the magnetizing inductance is a function of the V_g, V_o, β, and phase shift angle Φ. For the maximum Φ of $\pi/2$, and β of unity, maximum reduction in λ_{L_m} can be observed.

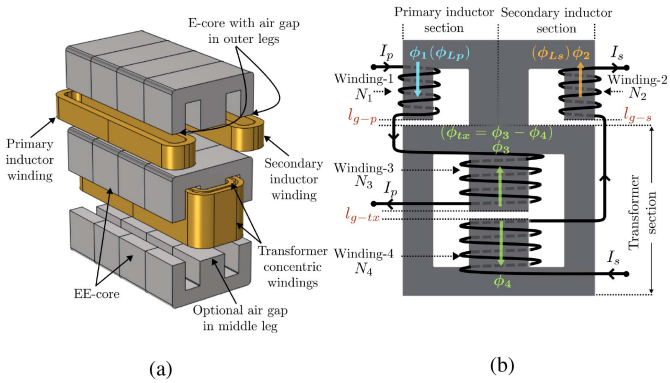

Fig. 4. 4W-ILX construction. (a) Exploded view. (b) 2-D view with a sense of winding and flux orientation.

From the above analysis, it can be concluded that the SL configuration allows for a higher degree of freedom in optimizing the performance parameters of the DAB converter by enabling independent tuning of L_1, L_2, and L_m values. However, in integrated magnetic structures reported in the state-of-the-art, incorporating series inductance (L or L_1, L_2) reduces L_m, or it is not possible to tune L_1 and L_2 independently. Conversely, using a discrete transformer with separate primary and secondary sides inductors guarantees decoupled tuning but results in increased volume and component count. To overcome this limitation, this work investigates whether it is possible to achieve independent tuning of L_1, L_2, and L_m in the integrated magnetic structure while achieving reduced volume and maintaining or improving converter efficiency compared to a discrete implementation.

III. Operation of 4W-ILX Structure for Dual Active Bridge Converter

The constructed 4W-ILX structure is shown in Fig. 4(a); it consists of an E-core with a gap on both the outer legs placed on top of the EE-core. EE-core middle leg can consist of an optional air gap, if control over L_m value is desired. E-core comprises primary and secondary inductor windings wound separately on each outer leg, and EE-core incorporates transformer windings, wound concentrically on the middle leg. Fig. 4(b) shows individual inductor and transformer sections of the core. Both the inductors and the transformer share the top yoke of the EE core. Winding-1 and winding-3 are connected in series and carry the primary side current I_p. Meanwhile, winding-2 and winding-4 are connected in series and carry the secondary side current I_s. Winding-1 and winding-4 are wound clockwise, generating flux ϕ_1 and ϕ_4 in the downward orientation for the shown current polarity, whereas winding-2 and winding-3 are wound anticlockwise, generating flux ϕ_2 and ϕ_3 in the upward orientation for the shown current polarity. N_1 to N_4 are turns

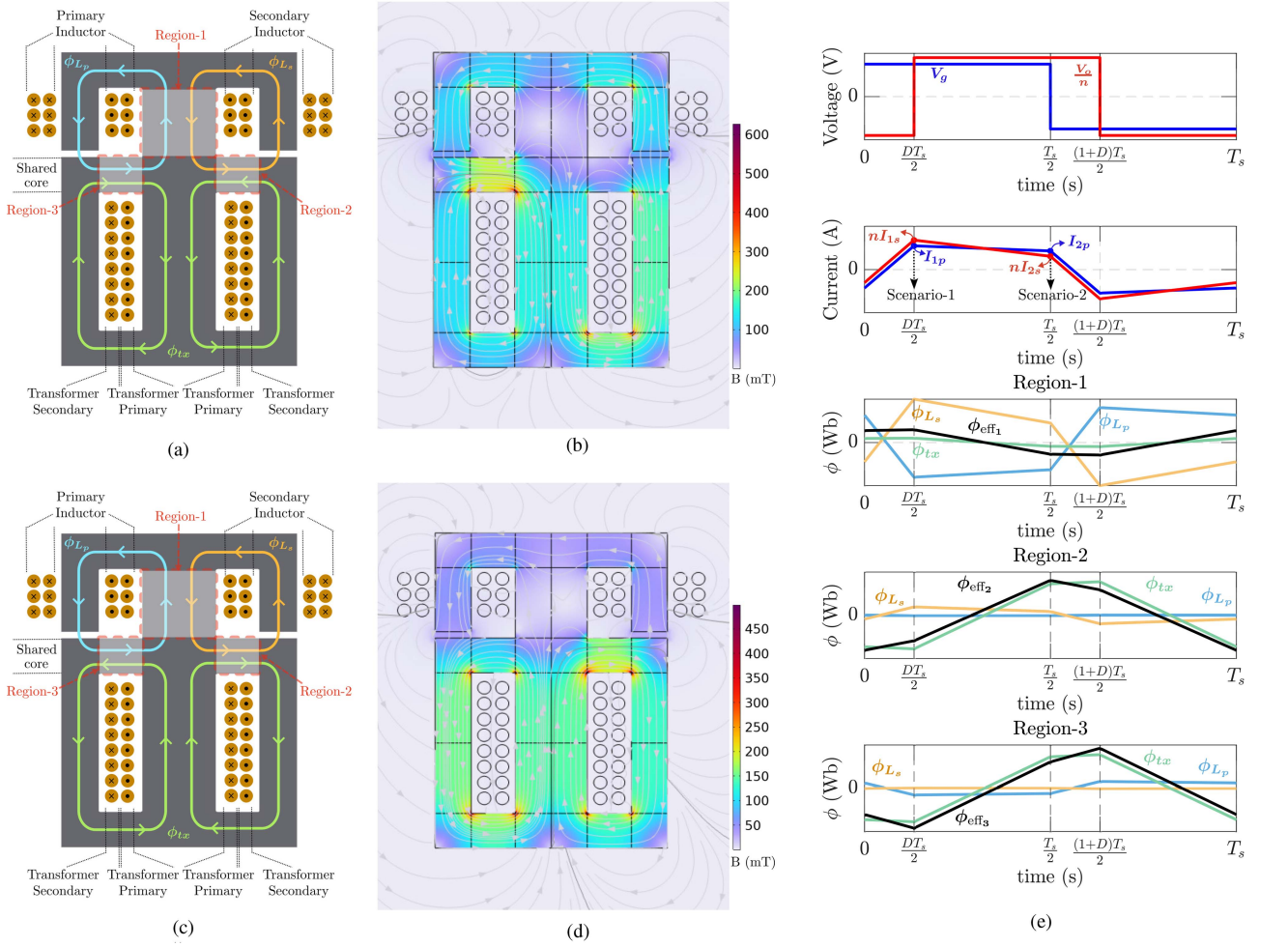

Fig. 5. 4W-ILX parameters: $\gamma = 26.34$, $\beta = 1$, $n = 0.5$ and $l_{g-tx} = 0$ (L_m not controlled). (a) Dominant decoupled flux path for scenario-1. (b) 2-D FEM flux density and flux direction result for scenario-1 at 450 V, 11 kW operating point. (c) Dominant decoupled flux path for scenario-2. (d) 2-D FEM flux density and flux direction result for scenario-2 at 450 V, 11 kW operating point. (e) Qualitative DAB converter current waveforms at the switching instant and flux waveforms in Region-1, Region-2, and Region-3.

of the winding-1 to winding-4, respectively. ϕ_{L_p} and ϕ_{L_s} are the primary and secondary inductor fluxes equivalent to ϕ_1 and ϕ_2, respectively. Likewise, ϕ_{tx} is transformer flux equivalent to $(\phi_3 - \phi_4)$. Air gap l_{g-p} and l_{g-s} on primary and secondary side of inductor E-core decouples ϕ_{tx} from ϕ_{L_p} and ϕ_{L_s}. In addition, the middle leg of the E-core acts as the lowest reluctance return path for ϕ_{L_p} and ϕ_{L_s}, minimizing the mutual coupling between them. The transformer section air gap is labeled l_{g-tx}.

A. Flux Distribution in 4W-ILX

The presence of finite magnetizing inductance alters the magnitude of current I_p and I_s at the switching instants, as described in Section II and shown in Fig. 5(e). This results in a change of magnitude of fluxes ϕ_3 and ϕ_4 leading to scenario-1 and scenario-2, as described as follows:

$$\begin{aligned} I_p < nI_s &\longrightarrow \phi_3 < \phi_4 \longrightarrow \text{scenario-1} \\ I_p > nI_s &\longrightarrow \phi_3 > \phi_4 \longrightarrow \text{scenario-2}. \end{aligned} \tag{6}$$

Fig. 5 shows 4W-ILX structure dominant flux paths, flux interactions in the shared core region, and corresponding 2-D magnetostatic FEM simulation results for the 450 V V_o and 11 kW P_o case. 4W-ILX parameters are $\gamma = 26.34$, $\beta = 1$, and $n = 0.5$. Note that the l_{g-tx} is considered as zero for the FEM simulation. It can be observed that during scenario-1, which occurs at switching instant $\frac{DT_s}{2}$, the magnitude of nI_{1s} dominates, and ϕ_{tx} flows in downward orientation. Conversely, for scenario-2, which occurs at $\frac{T_s}{2}$, magnitude of I_{2p} dominates and ϕ_{tx} flows in upwards orientation. This change in the orientation of ϕ_{tx} in one switching cycle leads to flux opposing and flux adding conditions in different regions of the 4W-ILX core.

Fig. 5(a) and (c) shows the dominant decoupled flux paths for scenario-1 and scenario-2, respectively. It can be observed that in Region-1, where ϕ_{L_p} and ϕ_{L_s} are dominant, the flux opposing condition occurs in both scenarios. However, in Region-2 and Region-3, the flux opposing and adding conditions between ϕ_{L_p} and ϕ_{tx}, and between ϕ_{L_s} and ϕ_{tx}, depend on the orientation of ϕ_{tx}. During scenario-1, in Region-2 fluxes ϕ_{L_s} and ϕ_{tx} opposes and in Region-3, fluxes ϕ_{L_p} and ϕ_{tx} adds. Likewise, for

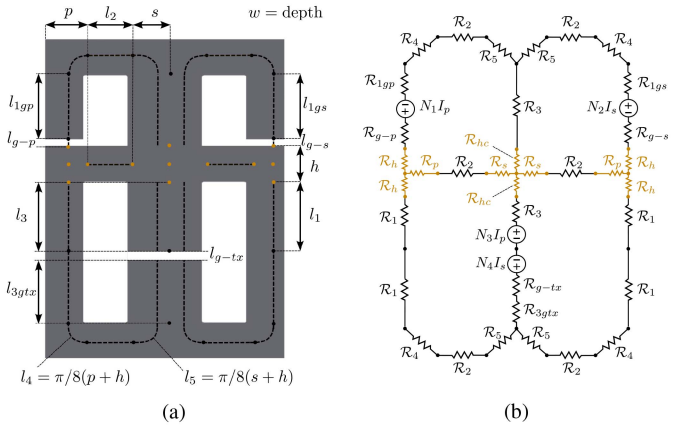

Fig. 6. (a) 4W-ILX core length dimensions. (b) 4W-ILX detailed reluctance model.

scenario-2, in Region-2 fluxes ϕ_{L_s} and ϕ_{tx} adds and in Region-3 fluxes ϕ_{L_p} and ϕ_{tx} opposes. Fig. 5(b) and (d) shows the flux density plot using a 2-D FEM simulation of a 4W-ILX structure. As seen from these plots, the flux density in Region-3 is higher for scenario-1, whereas the flux density of Region-2 is higher in the case of scenario-2. In both scenarios, the flux density of Region 1 is always lowest. This observation from the flux density plot supports the dominant flux distribution in these regions. To further see the effect of all the fluxes in the shared core regions, Fig. 5(e) shows the qualitative characteristics of these fluxes at the switching instant. The flux waveforms demonstrate that the effective flux ϕ_{eff_1} in Region-1, which is the sum of all the fluxes, is considerably reduced at both the switching instants. In Region-2, the effective flux ϕ_{eff_2} has lower magnitude at instant $\frac{DT_s}{2}$ compared to ϕ_{tx} and higher magnitude at instant $\frac{T_s}{2}$. Whereas, in Region-3, the effective flux ϕ_{eff_3} has slightly higher magnitude at instant $\frac{DT_s}{2}$ compared to ϕ_{tx}, and conversely lower magnitude at instant $\frac{T_s}{2}$. The effective fluxes ϕ_{eff_2} and ϕ_{eff_3} do not significantly reduce the peak-to-peak magnitude of ϕ_{tx} in their respective regions, and their contribution to reducing the overall core losses is minimal. The effective flux ϕ_{eff_1} in Region-1 consistently experiences opposing flux contributions and helps in the reduction of the core losses.

IV. Analytical Modeling of 4W-ILX Structure

The objective of analytical modeling is to estimate the self- and mutual inductances of a 4W-ILX that can be further used to derive DAB design parameters like effective current scaling ratio n_e, series inductances L_1 and L_2, and magnetizing inductance L_m. Fig. 6 shows the detailed reluctance model of 4W-ILX and the dimensions of the cores. Modeling the reluctance of the shared core region, particularly at the junction, is challenging because the flux splits into two paths, and its mean path length and cross-sectional area can change significantly with operating conditions. Therefore, to simplify the proposed reluctance model, two assumptions are made: (1) a constant core permeability, μ_r, is used when deriving the inductances, and (2) the shared-core segment is modeled using idealized geometric dimensions. The approximate reluctances in the shared core region are given by $\mathcal{R}_h$, $\mathcal{R}_p$, $\mathcal{R}_s$, and $\mathcal{R}_{hc}$, as shown in Fig. 6(b). These assumptions introduce a finite error but enable quick estimation of the key parameters. The air gap reluctances $\mathcal{R}_{g-p}$, $\mathcal{R}_{g-s}$, and $\mathcal{R}_{g-tx}$ are obtained using the 3-D air gap reluctance calculation method described in [25]. All the other reluctances are defined in Table II.

TABLE II
Reluctances and Cross-Sectional Areas of Core Segments in 4W-ILX

Reluctance	Reluctance	Cross-sectional Area
$\mathcal{R}_1 = \frac{l_1}{\mu_0\mu_r A_1}$	$\mathcal{R}_{1gs} = \frac{l_{1gs}}{\mu_0\mu_r A_1}$	$A_1 = pw$
$\mathcal{R}_2 = \frac{l_2}{\mu_0\mu_r A_2}$	$\mathcal{R}_{3gtx} = \frac{l_{3gtx}}{\mu_0\mu_r 2A_3}$	$A_2 = hw$
$\mathcal{R}_3 = \frac{l_3}{\mu_0\mu_r\, 2A_3}$	$\mathcal{R}_p = \frac{p/2}{\mu_0\mu_r A_2}$	$A_3 = sw$
$\mathcal{R}_4 = \frac{l_4}{\mu_0\mu_r A_4}$	$\mathcal{R}_s = \frac{s}{\mu_0\mu_r A_2}$	$A_4 = \frac{A_1 + A_2}{2}$
$\mathcal{R}_5 = \frac{l_5}{\mu_0\mu_r A_5}$	$\mathcal{R}_{hc} = \frac{h/2}{\mu_0\mu_r\, 2A_3}$	$A_5 = \frac{A_2 + A_3}{2}$
$\mathcal{R}_{1gp} = \frac{l_{1gp}}{\mu_0\mu_r A_1}$	$\mathcal{R}_h = \frac{h/2}{\mu_0\mu_r A_1}$	–

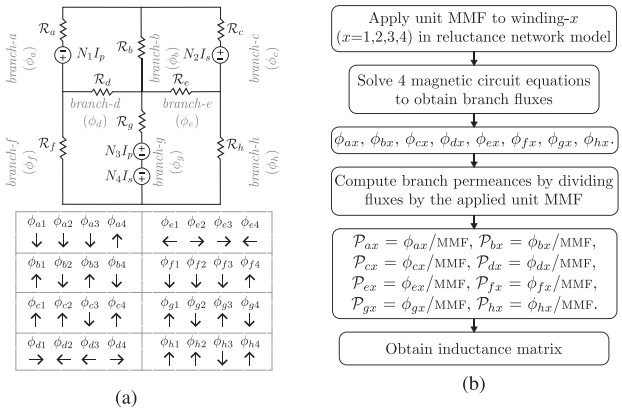

Fig. 7. (a) Simplified reluctance model and flux direction. (b) Method to obtain the inductance matrix.

A. Inductance Matrix of 4W-ILX Structure

Fig. 7 shows the simplified reluctance model and method to obtain the inductance matrix. The simplified reluctance model is derived by summing the reluctances in each branch of the detailed reluctance model. In Fig. 7(a) branches are labeled 'a' to 'h'. The fluxes in these branches are denoted as 'ϕ_a' through "ϕ_h". The orientation of the individual fluxes in each branch is also shown for the given current polarity; for instance, ϕ_{a1} is the downward flowing (↓) flux in branch-a, generated by winding-1. The first step is to determine the flux contribution of each winding by applying a unit magnetomotive force (MMF) source one at a time and solving four magnetic circuit equations. Once all the fluxes in each branch of the reluctance network model are determined for all the windings, the permeance of the space occupied by all these fluxes is obtained by dividing these fluxes by a unit MMF source. These permeances are then used to calculate the inductance matrix, as shown in (7). Where L_1

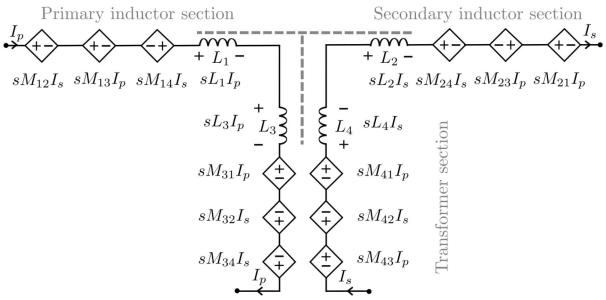

Fig. 8. Two-port coupled inductor model of the 4W-ILX structure.

and L_2 are the same as defined in Section II, and L_3 and L_4 are the self-inductance of the 4W-ILX transformer section primary and secondary windings, respectively.

Once the inductor matrix is obtained, the two-port coupled inductor model is constructed by using an inductor for the self-inductance term and dependent voltage sources for the coupling term, as shown in Fig. 8. This two-port coupled inductor model is used to determine the essential design parameters of the DAB converter

$$L = \begin{bmatrix} L_1 & M_{12} & M_{13} & M_{14} \\ M_{21} & L_2 & M_{23} & M_{24} \\ M_{31} & M_{32} & L_3 & M_{34} \\ M_{41} & M_{42} & M_{43} & L_4 \end{bmatrix} = \begin{bmatrix} N_1^2 P_{a1} & N_1 N_2 \mathcal{P}_{a2} & N_1 N_3 \mathcal{P}_{a3} & N_1 N_4 \mathcal{P}_{a4} \\ N_2 N_1 \mathcal{P}_{c1} & N_2^2 \mathcal{P}_{c2} & N_2 N_3 \mathcal{P}_{c3} & N_2 N_4 \mathcal{P}_{c4} \\ N_3 N_1 \mathcal{P}_{g1} & N_3 N_2 \mathcal{P}_{g2} & N_3^2 \mathcal{P}_{g3} & N_3 N_4 \mathcal{P}_{g4} \\ N_4 N_1 \mathcal{P}_{g1} & N_4 N_2 \mathcal{P}_{g2} & N_4 N_3 \mathcal{P}_{g3} & N_4^2 \mathcal{P}_{g4} \end{bmatrix}. \tag{7}$$

The effective current scaling ratio n_e given in (8) is used to determine primary and secondary current magnitudes, including the effect of coupling terms in 4W-ILX. It is derived by short-circuiting the secondary side of the transformer section, applying the KVL to the secondary side loop, and then taking current ratios. n_e is equivalent to physical turns ratio n when the coupling terms k_{41} and k_{42} are zero and k_{43} is unity

$$n_e = \frac{I_p}{I_s} = \frac{L_4 + M_{42}}{M_{43} + M_{41}}. \tag{8}$$

The magnetizing inductance of the 4W-ILX is determined by considering the secondary of the transformer section open ($I_s = 0$), and calculating the total inductance at the primary of the transformer section. The magnetizing inductance L_m is given by (9). The value of mutual inductance M_{31} is expected to be very low compared to L_2, and is verified further in Section V-C

$$L_m = L_3 + M_{31}. \tag{9}$$

The primary and secondary side series inductances are given by (10) and (11), respectively. They are obtained by adding the self-inductance and mutual inductance terms in their respective inductor section. The contribution of the mutual inductor term is negligible, and the value of the series inductance depends primarily on the self-inductance term, as shown further in Section V-C

$$L_p = L_1 + \frac{M_{12}}{n_e} + M_{13} - \frac{M_{14}}{n_e} \tag{10}$$

$$L_s = L_2 + M_{21} n_e - M_{23} n_e + M_{24}. \tag{11}$$

TABLE III
DAB CONVERTER SPECIFICATION

	Parameters	Values
DAB converter	Input voltage V_g	775 V
	Output voltage V_{o-min}-V_{o-max}	250 V-450 V
	Max. output current I_{o-max}	28 A
	Max. output power P_{o-max}	11 kW
	Operating frequency f_s	50 kHz
	Primary series inductor L_p	50 μH
	Secondary series inductor L_s	12.5 μH
	Magnetizing inductor L_m	High (not controlled)
	Turns ratio n	0.5
	γ, β	$\gg$ 1 (High) , 1
4W-ILX	Reduction factor δ	10 %
	Max. flux density in shared core $B_{\text{m,shared}}$	0.25 T
	Window packaging factor k_w	0.25
	Max. current density J_m	3 A/mm^2
	Apparent power VA	15 kVA

V. DESIGN METHOD OF 4W-ILX STRUCTURE FOR DAB CONVERTER

The analytical design method and air gap sensitivity analysis for the 4W-ILX structure are given in this section. Table III shows the design specifications of the DAB converter and 4W-ILX structure.

A. Transformer Core and Winding Selection

The value of the L_m parameter is not specified and expected to be high; therefore, the transformer design is based on a gapless EE core, where the value of l_{g-tx} is set to zero. In a 4W-ILX structure, the shared core regions, Region-2 and Region-3, carry both transformer and inductor fluxes. Therefore, the maximum flux density in the shared core region $B_{\text{m,shared}}$ becomes a critical limiting factor for designing the 4W-ILX. The transformer EE-core is sized based on the area product approach, and the maximum flux density value of $B_{\text{m,Tx}}$ is used in this method. $B_{\text{m,Tx}}$ is derived by scaling down $B_{\text{m,shared}}$ to incorporate the design margin when both the transformer and inductor fluxes add in the shared region. $B_{\text{m,Tx}}$ is calculated using (12), where δ is % reduction. In this work, a conservative design parameter of $\delta = 10\%$ is used

$$B_{\text{m,Tx}} \leq \frac{B_{\text{m,shared}}}{1+\delta}. \tag{12}$$

For the given parameters like volt-amp VA rating, operating frequency f_s, maximum current density J_m, window packaging factor k_w, and a calculated $B_{\text{m,Tx}}$, the area product A_p is given as follows:

$$A_p = \frac{\text{VA}}{2 f_s k_w J_m B_{\text{m,Tx}}}. \tag{13}$$

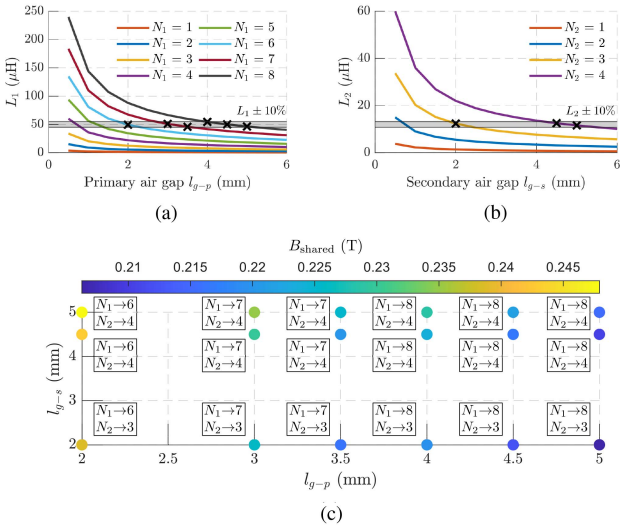

Fig. 9. (a) Parametric sweep for L_1. (b) Parametric sweep for L_2. (c) Shared core flux density $B_{\text{m,shared}}$ value for the selected combinations of primary and secondary air gaps and turns.

An appropriate EE-core size having an area product greater than the calculated A_p is chosen for the transformer section. Litz wire windings are used on primary and secondary, and the number of strands n_s and strand diameter d_s are selected based on the maximum current density J_m and the skin depth criteria. The number of turns is selected based on the V_{o-max} as a conservative assumption, since the design targets a high L_m. Turns N_3 and N_4 are calculated using (14), where A_c is the cross-sectional area of the core. The maximum number of turns is limited by the window area of the EE-core, the window packaging factor k_w, and the Litz wire's cross-section area A_{litz}

$$N_3 = \frac{V_{o-max}}{4A_c B_{\text{m,Tx}} f_s} \qquad N_4 = N_3/n. \tag{14}$$

Based on the above equations and the given design parameters, 4 parallel E70-33-32 cores are selected for the 4W-ILX transformer section, and the number of turns N_3 and N_4 are calculated as 8 and 4, respectively.

B. Inductor Air Gap and Turns

The inductor section consists of an E-core of the same dimensions as that of the transformer core, so that their legs align vertically when stacked. The self-inductances L_1 and L_2 can be tuned by varying their respective air gaps l_{g-p} and l_{g-s}, as well as the winding turns N_1 and N_2. The selection of air gap length and turns depends on the expected inductance value and $B_{\text{m,shared}}$. Since the fluxes of both the primary and secondary inductors are decoupled, the selection of air gap length and turns for each inductor can be done independently to match the expected inductance value, as shown in Fig. 9(a) and (b). The analytical model is used for a parametric sweep. The maximum number of turns is based on the window area of the inductor E-core, k_w, and A_{litz}. The air gap is varied in steps of 0.5 mm, and the maximum air gap length of 6 mm is considered. The air gap and turns combinations that yield the self-inductance value in the range of $\pm 10\%$ are selected. While carrying out a parametric sweep for L_1, the l_{g-s} is set to a constant minimum length of 0.5 mm and vice versa.

These selected combinations of air gap and turns for both L_1 and L_2 inductors are then qualified by evaluating their shared core flux density B_{shared} using an analytical model at the worst-case operating point, in this case with the excitation currents at V_o of 450 V and P_o of 11 kW. Fig. 9(c) shows the selected combination of primary and secondary air gap and turns, and their respective B_{shared} values. All the selected combinations qualify as their resulting shared core flux density is below the given $B_{\text{m,shared}}$ value. Among these combinations, the one chosen for this design consists of l_{g-p} and l_{g-s} of 2 mm, and N_1 and N_2 of 6 and 3, respectively. This combination meets the shared core flux density and inductance criteria, as well as requires a minimum number of turns for both the primary and secondary inductors. Table IV summarizes the design outcomes for 4W-ILX.

TABLE IV
4W-ILX DESIGN OUTCOMES

Parameters	Values
Core size	E70-33-32 (4×EE for Tx, 4×E for L)
Core material	N27, B_{sat} = 0.41 T @ 100°C, μ_r = 1500
Air gap	$l_{g-p} = l_{g-s}$ = 2 mm
Turns	N_1 = 6, N_2 = 3, N_3 = 8, N_4 = 4
Litz wire	A_{litz} = 12.2 mm^2, d_s = 0.2 mm , n_s = 200
Winding arrangement	Winding 1→ 2 layer, Winding 2→ 2 layer, parallel Winding 3→ 1 layer, Winding 4→ 1 layer parallel
Analytical	
Self-inductance	L_1 = 49.48 μH, L_2 = 12.37 μH L_3 = 2.1 mH, L_4 = 529.7 μH
γ, β	21.22 , 1
FEM	
Self-inductance	L_1 = 45.93 μH, L_2 = 11.48 μH L_3 = 2.42 mH, L_4 = 606.83 μH
γ, β	26.34 , 0.99

C. Air Gap Sensitivity Analysis for 4W-ILX Structure

The air gap sensitivity analysis is performed using FEM simulation to validate that L_m, L_p, and L_s can be tuned independently. This analysis also shows the coupling effect on these parameters, as highlighted in (9), (10), and (11).

Fig. 10(a) shows the variation of l_{g-p}, by keeping l_{g-s} as 2 mm and l_{g-tx} as 0 mm. It can be observed that the value of L_1 varies significantly with the l_{g-p}, but the variation in L_2 is negligible; this is also verified as the values of k_{12}, k_{21} are close to zero. The variation in l_{g-p} leads to a small increment in the value of L_m around 2.8% and converges to L_3 as the air gap increases. Compared to other leakage inductance integration methods, where L_m decreases with higher values of leakage inductances [6], [7], [8], [9], [10], [11], [12], [13], [14], in 4W-ILX, L_m value slightly increases with the higher values of L_1. The coupling between transformer windings k_{34}, k_{43} remains substantially high, independent of L_1 value, indicating lower

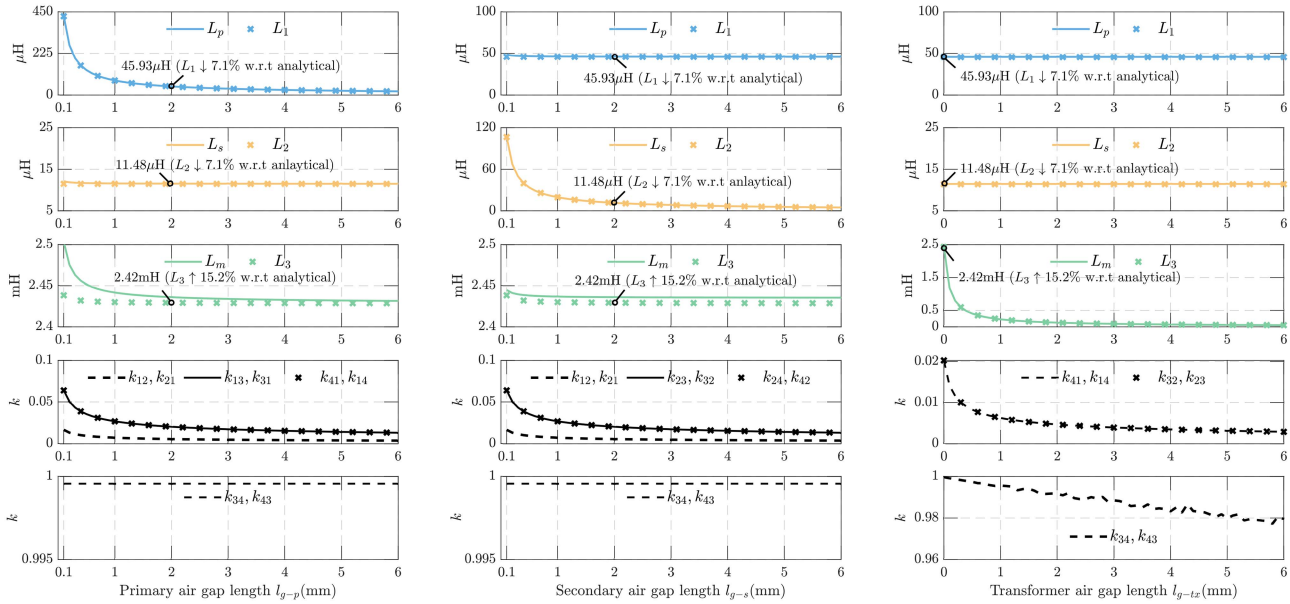

(a) (b) (c)

Fig. 10. Effect of air–gap variation on L_m, L_p, L_s, and coupling coefficients of 4W-ILX. (a) l_{g-p} is varied while $l_{g-s} = 2$ mm and $l_{g-tx} = 0$ mm. (b) l_{g-s} is varied while $l_{g-p} = 2$ mm and $l_{g-tx} = 0$ mm. (c) l_{g-tx} is varied while $l_{g-p} = 2$ mm and $l_{g-s} = 2$ mm.

leakage fluxes. In addition to this, it can be observed that the difference between L_1 and L_p as well as the difference between L_2 and L_s is negligible due to a very small coupling effect. Moreover, a similar sensitivity analysis is performed by varying l_{g-s}, while keeping the value of l_{g-p} as 2 mm and l_{g-tx} as 0 mm, as shown in Fig. 10(b). The value of L_2 varies substantially with the l_{g-s}, and there is a negligible change in the value of L_1. In this case, the L_m variation with l_{g-s} is even smaller, around 0.37%. The coupling between transformer windings is not affected by the integration of L_2 as the values of k_{34}, k_{43} are close to unity. Finally, Fig. 10(c) shows, the variation in l_{g-tx} by keeping value of both l_{g-p} and l_{g-s} as 2 mm, to demonstrate that the value of L_m can also be controlled and can be intentionally lowered by increasing the l_{g-tx} parameter. It is also observed that the value of L_1 and L_2 does not vary with l_{g-tx}, but the value of L_m substantially decreases. This ensures that L_m can be controlled without influencing L_1 and L_2, which is not possible in the asymmetric windings integration method [10], [15], [16]. The coupling between the transformer primary and secondary windings k_{34}, k_{43} is slightly lowered due to increased leakage flux caused by higher air-gap fringing.

It is important to note that the finite air gap length for l_{g-p} and l_{g-s} is required in 4W-ILX to enable precise control of inductance value and allow the inductor to operate at high values of current without saturation, whereas air-gap length l_{g-tx} is optional. The difference between the analytically obtained and FEM based self-inductance values, L_1 and L_2, is within 10%, whereas for L_3, it is higher than 10% due to the assumption made in the reluctance-based 4W-ILX modelling in Section IV; the corresponding FEM-derived values are listed in Table IV.

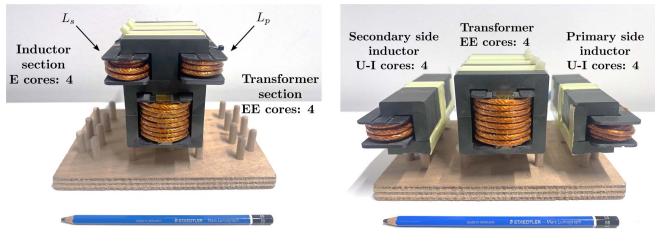

(a) (b)

Fig. 11. (a) 4W-ILX structure. (b) Discrete inductors and transformer structures.

VI. Experimental Results

This section presents the experimental evaluation of the proposed 4W-ILX structure in terms of its physical, electrical, and thermal performance metrics. Furthermore, it provides a comparative assessment on the same metrics against a discrete implementation, comprising separate primary and secondary inductors and a transformer, to quantify the reduction in magnetic volume while maintaining or improving DAB converter efficiency.

A. Physical Construction and Electrical Characteristics of Both Magnetic Structures

Fig. 11 shows the physical construction of 4W-ILX and the discrete structures used in the experimental comparison with the identical electrical values. The discrete magnetic implementation comprises separate U-I cores for primary and secondary side inductors. Both discrete inductors consist of the same air

TABLE V
EXPERIMENTALLY MEASURED ELECTRICAL PARAMETERS AND INSULATION CLASSES OF MAGNETIC STRUCTURES

	Parameters	Discrete Structure	ILX Structure
Measured Electrical Parameter	L_1	44.89 μH	44.32 μH
	L_2	10.35 μH	10.84 μH
	L_3	2.45 mH	2.49 mH
	L_4	614.27 μH	629.26 μH
	M_{12}, M_{21}	N/A	0.253 μH
	M_{13}, M_{31}	N/A	4.10 μH
	M_{14}, M_{41}	N/A	2.43 μH
	M_{23}, M_{32}	N/A	2.25 μH
	M_{24}, M_{42}	N/A	1.11 μH
	M_{43}, M_{34}	1.24 mH	1.25 mH
	Transformer leakage	2.99 μH	3.02 μH
	Core volume	774.456 cm^3	672.979 cm^3
	Total volume	1378.753 cm^3	1211.321 cm^3
	Total weight	4323 g	3916 g
	Power density	8.05 kW/L	9.16 kW/L
Insulation Class	Litz wire	Class 200	Class 200
	Coil former	PET-CF (205°C)	PET-CF (205°C)
	Polyimide tape	Class 220	Class 220
	Polyester film tape	130°C	130°C
	Polyamide 46 tie	150°C	150°C

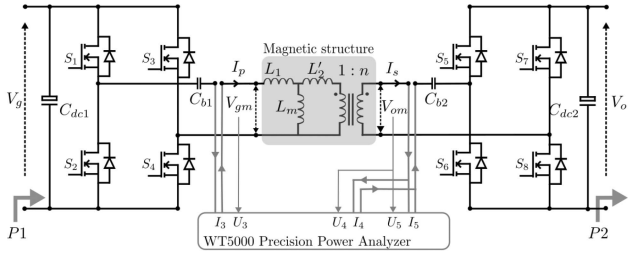

Fig. 12. Electrical connection schematic for measurements.

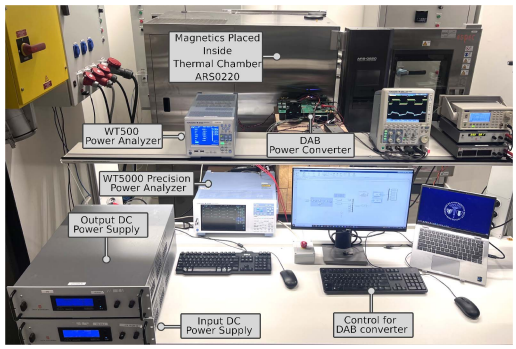

Fig. 13. Layout of the experiment setup.

gap length as the 4W-ILX inductors to ensure a fair comparison. The total volume of primary and secondary U-cores used in the discrete inductor matches the volume of the E-cores used in the inductor section of 4W-ILX. The additional I-cores are required in the discrete inductor structures to complete the magnetic circuit, which increases their overall core volume. The discrete transformer constructed using the EE-cores has the same volume as that of the 4W-ILX transformer section. The number of turns, Litz wire specifications, and winding arrangement used in the discrete inductors and the transformer are identical to the 4W-ILX structure, as listed in Table IV.

The electrical parameters of 4W-ILX and discrete structures are measured using a KEYSIGHT E4990 A impedance analyzer and are listed in Table V. The measured self-inductances of both structures are within a 5% margin. The mutual inductance of 4W-ILX, obtained from the measurements, shows a weak coupling between the primary and secondary side inductor windings k_{12}, k_{21}= 0.0116. Likewise, the mutual inductances between both the inductor windings and the transformer windings also indicate weak coupling. k_{13}, k_{31}= 0.0123 and k_{14}, k_{41}= 0.0146 for primary inductor winding and transformer windings. Similarly, k_{23}, k_{32}= 0.0135 and k_{24}, k_{42}= 0.0137 for secondary inductor winding and transformer windings. Whereas, the coupling between the 4W-ILX transformer's primary and secondary winding remains high k_{34}, k_{43} = 0.9988. These measurements validate the FEM based analysis shown in Section V-C. The leakage inductance of both structures has a similar value, and therefore, their effect on power transfer and losses is considered equal.

The physical construction of the proposed 4W-ILX structure shows that the total volume reduction of 12.1% and the total weight reduction of 9.4% are achieved compared to a discrete structure. The volume calculation is done based on the bounded box around the magnetic structures, which includes the core, winding window area, windings, and bobbin. The insulation class of the materials used in both magnetic structures is listed in Table V. These classes define the permissible temperature limits, and maintaining operating temperature within these limits ensures long-term reliability.

B. Experimental Setup

This section presents the experimental setup and comparative performance of the 4W-ILX structure and discrete structures under identical electrical and thermal conditions. Figs. 12 and 13 show the electrical connections and actual layout of the experiment setup, respectively. A DAB converter with a 4W-ILX structure equivalent to a split inductance configuration is shown. The input voltage V_g and output voltage V_o of the DAB converter are controlled using dc power supplies.

The losses are measured using a YOKOGAWA WT5000 precision power analyzer. The magnetic structure's input voltage V_{gm} and current I_p are measured by channel-3. Whereas the output voltage V_{om} and current I_s of the magnetic structure are measured by paralleling channel-4 and channel-5. This parallel arrangement is done to avoid exceeding the current limit of the power analyzer. For each comparative test, the output voltage V_o and the output power P_o of the power converter are maintained at constant values. Additionally, the ambient temperature is maintained with the help of the environmental

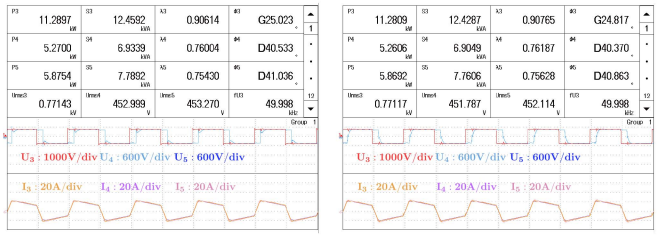

Fig. 14. WT5000 power analyzer data at 450 V, 11 kW, and 25 °C test condition. (a) 4W-ILX structure. (b) Discrete structures.

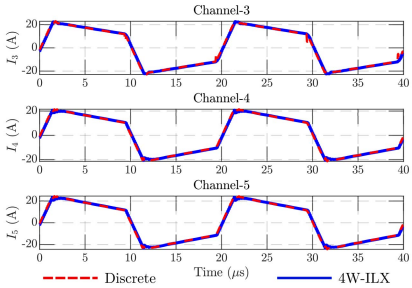

Fig. 15. Overlay of WT5000 captured input (I_3) and output (I_4, I_5) excitation current of magnetic structures.

test chamber ARS0220 throughout the test for fair comparison. Both 4W-ILX and discrete structures are tested at different ambient temperatures (i.e., 25°C, 16°C, and 4°C). The power loss measurements using a power analyzer are made when the magnetic structures attain a steady-state temperature to ensure stable core and winding loss measurements.

C. Comparative Test Measurements

The comparative test at rated high voltage and high power conditions (450 V, 11 kW) is presented in detail in this section. This operating point shows the worst-case thermal and electrical stress condition, making it critical to evaluate the loss characteristics of the 4W-ILX and discrete magnetic structures. The ambient temperature of 25°C is maintained by the thermal chamber during continuous operation. Fig. 14 presents the WT5000 power analyzer data for loss evaluation. Based on Fig. 14, the power loss dissipation of 4W-ILX, $P_{loss,4W\text{-}ILX}$ is 144.30 W, and the power loss dissipation of the discrete structure, $P_{loss,Disc}$ is 151.10 W at steady state thermal conditions. This represents about 4.5% (6.8 W) reduction in losses using the proposed 4W-ILX structure while achieving the total volume reduction of 12.1%. The absolute power loss values measured using WT5000 include a tolerance error. However, since the magnetic loss differences $\Delta P_{loss,mag}$ between 4W-ILX and the discrete structure are small under identical test conditions, the measurement tolerances are assumed to be similar for both cases and do not significantly affect the relative comparison. To demonstrate that the excitation currents are nearly identical, Fig. 15 shows an overlay of input and output currents for 4W-ILX and the discrete structures, taken from the WT5000 power analyzer during individual tests. Furthermore, the core and

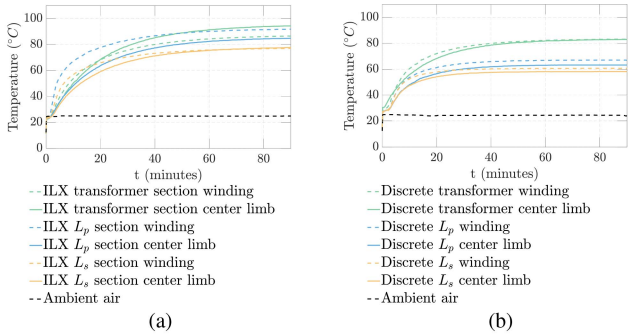

Fig. 16. Thermocouple data at 450 V, 11 kW, and 25°C test condition. (a) 4W-ILX structure. (b) Discrete structures.

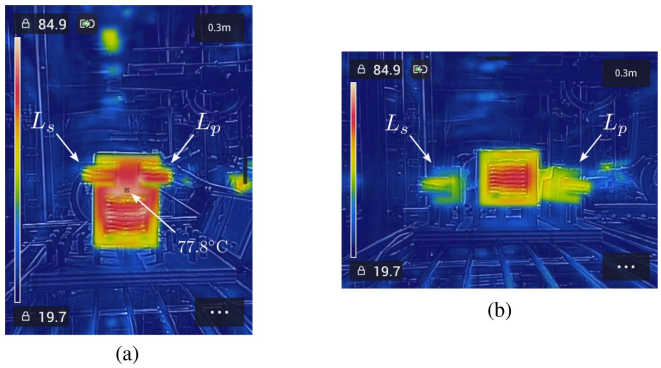

Fig. 17. Infrared thermal image at 450 V, 11 kW, and 25°C test condition ($\varepsilon = 0.95$, 0.3 m). (a) 4W-ILX structure. (b) Discrete structures.

winding temperatures of both 4W-ILX and discrete structures are measured using the thermocouples to identify hot spots and the thermal equilibrium state of each magnetic structure. The thermocouples are mounted on the center leg of the core and in the center region of the winding to measure the worst-case core and winding temperatures. The thermocouple measured data from Fig. 16 reveal that 4W-ILX has an overall higher temperature profile than discrete structures. The temperature difference between the 4W-ILX and discrete component is 21.6 °C for the transformer core, 19.5 °C for the secondary inductor core, and 11.4 °C for the primary inductor core, with the 4W-ILX being hotter in all cases. This elevated temperature profile is primarily due to the flux-adding condition in the shared core Region-3 and Region-2 during scenario-1 and scenario-2, respectively, as shown in Fig. 5(b) and (d). The higher flux density in these regions results in localized losses and hotspots. Moreover, due to its vertical stack cores and reduced volume, 4W-ILX has a lower surface area for convection cooling, resulting in a higher average temperature. Despite this temperature rise, the 4W-ILX remains within insulation class limits during its operation.

To visualize the temperature distribution across the 4W-ILX and the discrete core structures, an infrared thermal imaging camera, FLIR C5, is used. Fig. 17 shows the steady-state thermal images of both magnetic structures captured inside the thermal chamber. From Fig. 17(a), it is observed that the hotspot in the shared core region between the inductor section and the transformer section is visible, with a maximum surface temperature of

TABLE VI
COMPARATIVE TEST RESULTS

Operating Point (V_o, P_o)	Controlled ambient Temp (°C)	Discrete Structure $P_{loss,Disc}$* (W)	ILX Structure $P_{loss,4W\text{-}ILX}$* (W)	Magnetic $\Delta P_{loss,mag}$† (W)	Converter-Discrete $P_{conv,Disc}$ (W)	Converter-ILX $P_{conv,4W\text{-}ILX}$ (W)	Converter ΔP_{conv} (W)
450 V, 11 kW	25	151.10	144.30	6.80	320.00	314.00	6.00
	4	164.70	151.40	13.30	323.00	312.00	11.00
450 V, 7 kW	25	117.30	111.40	5.90	189.00	182.00	7.00
	4	130.30	122.70	7.60	198.00	189.00	9.00
385 V, 7 kW	25	88.69	86.45	2.24	159.00	157.00	2.00
	16	94.50	94.00	0.50	161.00	161.00	0.00
250 V, 7 kW	25	7.12	6.65	−0.59	229.00	235.00	6.00
	16	17.89	10.08	7.81	233.00	241.00	8.00

* Reported absolute loss values are based on direct WT5000 measurements and do not include tolerance estimation.
† Loss differences ($\Delta P_{loss,mag}$) are small, WT5000 measurement tolerances are assumed to be similar under identical conditions.

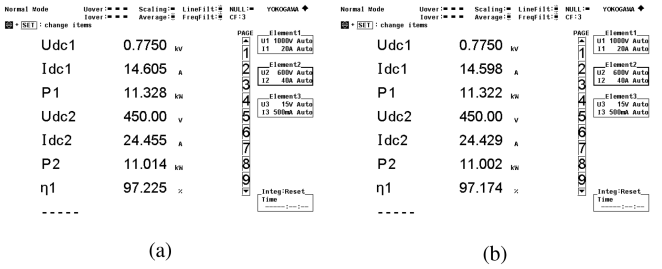

(a) (b)

Fig. 18. Snapshot of power analyzer measuring the DAB converter efficiency at 450 V, 11 kW, and 25 °C test conditions. (a) 4W-ILX structure. (b) Discrete structures.

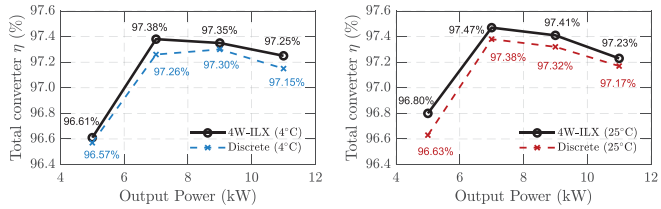

(a) (b)

Fig. 19. Measured DAB converter efficiency at 450 V operation with 4W-ILX and discrete structures for wide operating power at ambient temperature of (a) 4 °C and (b) 25 °C.

around 77.8 °C. This location of the hotspot is consistent with the thermocouple measurement, as shown in Fig. 16. In addition, the thermal coupling between the inductor and transformer sections of the 4W-ILX core results in temperature redistribution. This lowers the internal temperature gradient between the hottest and coolest regions of the core. In contrast, the discrete structure, though operating at a lower maximum temperature, shows a higher temperature gradient between the individual components as they dissipate heat independently.

Furthermore, the overall DAB converter efficiency is evaluated using a YOKOGAWA WT500 power analyzer by measuring the converter's input and output port power levels, P1 and P2, respectively, to study the impact of the 4W-ILX structure with respect to discrete structures. Fig. 18 shows the image of the measured power and efficiency for both 4W-ILX and the discrete magnetic structures. It can be observed that the output voltage and power are maintained at a similar level for both magnetic structures, ensuring a fair comparison. A slightly higher output power in 4W-ILX is due to the limited resolution of the duty cycle control. Under steady-state thermal conditions, the converter level losses are 314 W for the 4W-ILX configuration ($P_{conv,4W\text{-}ILX}$) and 320 W for the discrete configuration ($P_{conv,Disc}$), resulting in converter level loss difference (ΔP_{conv}) of 6 W. This result aligns and validates the comparative magnetic power loss measurements using the WT5000 precision power analyzer.

Table VI summarizes the magnetic and converter performance over a wide range of operating voltages and output power levels under different ambient temperatures. The 25°C test represents the typical operating condition, while the additional tests at 16°C and 4°C are conducted to compare the relative performance of the structures. For both 450 V and 385 V output voltages, the 4W-ILX structure consistently achieves lower magnetic losses and lower converter-level losses compared to the discrete configuration. However, at 250 V, 7 kW, and ambient temperature of 25 °C, the measured $\Delta P_{loss,mag}$ obtained using the WT5000 is –0.59 W. This negative value arises from the very small absolute losses and high reactive power in this operating region, both of which increase the measurement uncertainty of the WT5000 analyzer. Nevertheless, the converter level performance measured using the WT500 confirms that the 4W-ILX structure maintains higher efficiency than the discrete design.

In addition, Fig. 19(a) and (b) compares the DAB converter efficiencies of the 4W-ILX and discrete structures at various output power levels for 450 V output voltage, under controlled ambient temperatures of 4 °C and 25 °C, respectively. The results indicate that the 4W-ILX magnetic structure achieves equal or higher efficiency across the evaluated power range for both ambient temperatures.

D. Loss Breakdown of Proposed 4W-ILX and Comparison With Discrete Structure

The loss breakdown of the DAB converter with proposed 4W-ILX and discrete structure at 450 V and 11 kW power is shown in Fig. 20(a), and power losses in 4W-ILX at 450 V and at different output power levels is shown Fig. 20(b). The core and winding losses are computed using FEM-obtained B and H field data and analytical loss models. Improved Generalized Steinmetz Equation [26] is used for core loss calculations, and

TABLE VII
COMPARISON OF PROPOSED 4W-ILX STRUCTURE WITH EXISTING INTEGRATED STRUCTURES IN DAB

Items	Specification of DAB				Converter η_{P_o-max} (%)	Converter η_{peak} (%)	Load and voltage at peak efficiency	Magnetic integration type	Ambient temperature
	$P_o - max$ (W)	V_g (V)	V_o (V)	f_s (kHz)					
This work	11000	775	250-450	50	97.23	97.81	7000 W, 385 V	Split inductor integrated magnetics	25°C (controlled)
[13]	18.5	20	20	100	91.70	–	–	Integrated transformer	25°C
[17]	1000	300	18-36	150	94.10	96.40	600 W, 36 V	PCB-based dual transformer integration	-
[9]	1200	400	50	1000	95.60	97.51	843 W, 50 V	PCB-based integrated magnetics	-
[23]	6000	400	400	20	97.55	98.60	1800 W, 400 V	Orthogonal decoupling integrated magnetics	-

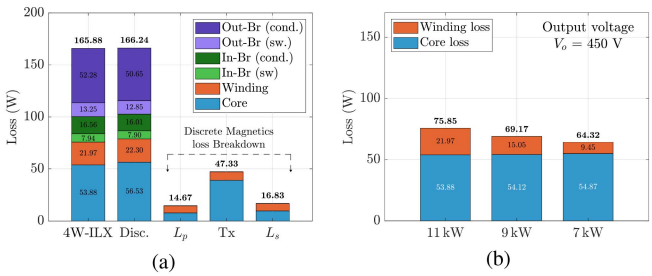

Fig. 20. Analytical loss evaluation. (a) Converter level loss breakdown for 4W-ILX and discrete (Disc.) structures at 450 V, 11 kW. (b) 4W-ILX structure core and winding losses at 450 V and at different output power levels.

the model proposed in [27] is used for calculating dc, skin effect, and proximity losses of Litz wire windings. The loss evaluation accounts for temperature-dependent core and winding parameters. Furthermore, semiconductor switching loss and conduction losses are evaluated using PLECS simulation.

E. Comparison of Proposed 4W-ILX With Existing Integrated Structures in DAB Converters

Table VII compares the proposed 4W-ILX structure with various state-of-the-art integrated magnetic designs reported in the literature for DAB converters. This comparison is based on several parameters, such as the specification of DAB, converter efficiency at maximum output power (η_{P_o-max}), converter peak efficiency (η_{peak}), output power and voltage at peak efficiency, type of magnetic integration used, and ambient temperature at which the test has been performed.

From Table VII, it can be seen that the design reported in [13] employs an integrated transformer structure operating at 100 kHz with a very low output power and voltage of 18.5 W and 20 V, respectively, achieving η_{P_o-max} of 91.70% at an ambient temperature of 25° C. The work in [17] presents a PCB-based dual transformer integration operating at 150 kHz with η_{peak} of 96.40% at 600 W of output power and 36 V output voltage. In [9], a PCB-based integrated magnetic structure operating at 1 MHz achieves η_{peak} of 97.51% at an output power and output voltage of 843 W and 50 V, respectively. In [23], DAB with orthogonal decoupling integrated magnetics achieves η_{P_o-max} of 97.55% at 20 kHz switching frequency and η_{peak} of 98.60% at 1.8 kW output power and 400 V output voltage. However, the ambient temperature for the designs in [9], [17], and [23] has not been reported, making direct thermal performance comparison difficult, since temperature strongly influences magnetic losses and overall efficiency. In contrast, the proposed 4W-ILX structure achieves $\eta_{P_o\text{-}max}$ of 97.23% at an output power of 11 kW and 450 V output voltage, and η_{peak} of 97.81% at 7 kW and 385 V output voltage, operating at 50 kHz under a controlled ambient temperature of 25°C. Compared with existing integration methods, the proposed 4W-ILX structure offers a balanced trade-off among efficiency, power scalability, and independent tuning of L_p, L_s, and L_m.

VII. CONCLUSION

In this article, a 4W-ILX magnetic structure has been proposed for a DAB converter to minimize the volume of magnetics while maintaining or improving the DAB converter efficiency compared to its discrete magnetic structures. The proposed magnetic structure integrates primary and secondary side series inductances with transformer functionality, providing decoupled operation and independent tuning. A design methodology based on the analytical model, derived using the reluctance, has been given for the 4W-ILX structure. Moreover, sensitivity analysis is performed using FEM simulation to verify the decoupling operation and is subsequently validated through experimental measurements. The electrical and thermal performance of the proposed 4W-ILX and the discrete magnetics structures have been experimentally evaluated and compared for a wide operating range under identical voltage, power, and temperature conditions (i.e., 250–450 V, 5–11 kW, and different ambient temperatures). The proposed 4W-ILX achieved a 12.1% reduction in volume and a total magnetic loss reduction of 4.5% at a rated power of 11 kW, output voltage of 450 V, and typical ambient temperature of 25 °C. In addition, the efficiency of the DAB converter has been evaluated using both the 4W-ILX and discrete structures across the full operating range. The results have shown that the 4W-ILX has consistently maintained equal or higher performance compared to the discrete structures. The 4W-ILX structure offers a higher degree of design freedom to optimize DAB converter performance while reducing volume and footprint, which can benefit EV applications. The future work aims to reduce the hotspots by thermal modeling of 4W-ILX and implementing a cooling strategy.

ACKNOWLEDGMENT

The project was carried out with a Top Sector Energy subsidy from the Ministry of Economic Affairs and Climate, carried out by the Netherlands Enterprise Agency (RVO). The specific subsidy for this project concerns the MOOI subsidy round 2020.

REFERENCES

[1] J. Chen, M. Nguyen, Z. Yao, C. Wang, L. Gao, and G. Hu, "DC-DC converters for transportation electrification: Topologies, control, and future challenges," *IEEE Electrific. Mag.*, vol. 9, no. 2, pp. 10–22, Jun. 2021.

[2] A. Hanson and D. Perreault, "Modeling the magnetic behavior of N-winding components: Approaches for unshackling switching superheroes," *IEEE Power Electron. Mag.*, vol. 7, no. 1, pp. 35–45, Mar. 2020.

[3] S. Yin, S. Debnath, R. Wojda, P. Marthi, and M. Saeedifard, "Impact of the transformer magnetizing inductance on the performance of the dual-active bridge converter," in *Proc. IEEE 22nd Workshop Control Model. Power Electron.*, Cartagena, Colombia, 2021, pp. 1–7.

[4] Y. Xiao, Z. Zhang, M. Andersen, and K. Sun, "Impact on ZVS operation by splitting inductance to both sides of transformer for 1-MHz GaN based DAB converter," *IEEE Trans. Power Electron.*, vol. 35, no. 11, pp. 11988–12002, Nov. 2020.

[5] M. Iyer, "An approach towards extreme fast charging station architecture for electric vehicles with partial power processing," in Ph.D. thesis, Electrical Engineering, North Carolina State Univ., Raleigh, NC, USA, 2020, [Online]. Available: https://repository.lib.ncsu.edu/items/2bf0b9de-e56d-4bb7-9d6a-b5a166bea293

[6] G. Ortiz, J. Biela, and J. Kolar, "Optimized design of medium frequency transformers with high isolation requirements," in *Proc. 36th Annu. Conf. IEEE Ind. Electron. Soc.*, Glendale, AZ, USA, 2010, pp. 631–638.

[7] M. Mu, L. Xue, D. Boroyevich, B. Hughes, and P. Mattavelli, "Design of integrated transformer and inductor for high frequency dual active bridge GaN charger for PHEV," in *Proc. IEEE Appl. Power Electron. Conf. Expo.*, Charlotte, NC, USA, 2015, pp. 579–585.

[8] B. Cougo and J. W. Kolar, "Integration of leakage inductance in tape wound core transformers for dual active bridge converters," in *Proc. Conf. Integr. Power Electron. Syst.*, Nuremberg, Germany, 2012, pp. 1–6.

[9] Z. Zhang, J. Huang, and Y. Xiao, "GaN-based 1-MHz partial parallel dual active bridge converter with integrated magnetics," *IEEE Trans. Ind. Electron.*, vol. 68, no. 8, pp. 6729–6738, Aug. 2021.

[10] T. Yuan, F. Jin, Z. Li, C. Zhao, and Q. Li, "Design of an integrated transformer with parallel windings for a 30-kW LLC resonant converter," *IEEE Trans. Power Electron.*, vol. 38, no. 11, pp. 14317–14333, Nov. 2023.

[11] M. Pavlovsky, S. Haan, and J. Ferreira, "Winding losses in high-current, high-frequency transformer foil windings with leakage layer," in *Proc. 37th IEEE Power Electron. Spec. Conf.*, Jeju, Korea (South), 2006, pp. 1–7.

[12] J. Biela and J. Kolar, "Analytic model inclusive transformer for resonant converters based on extended fundamental frequency analysis for resonant converter-design and optimization," *IEEJ Trans. Ind. Appl.*, vol. 126, no. 5, pp. 568–577, 2006.

[13] E. Lee, J. Park, M. Kim, and S. Han, "An integrated transformer design with a center-core air-gap for DAB converters," *IEEE Access*, vol. 9, pp. 121263–121278, 2021.

[14] J. Zhang, Z. Ouyang, M. Duffy, M. Andersen, and W. Hurley, "Leakage inductance calculation for planar transformers with a magnetic shunt," *IEEE Trans. Ind. Appl.*, vol. 50, no. 6, pp. 4107–4112, Nov.–Dec. 2014.

[15] B. Li, Q. Li, and F. Lee, "High-frequency PCB winding transformer with integrated inductors for a bi-directional resonant converter," *IEEE Trans. Power Electron.*, vol. 34, no. 7, pp. 6123–6135, Jul. 2019.

[16] R. Gadelrab and F. Lee, "PCB-based magnetic integration and design optimization for three-phase LLC," *IEEE Trans. Power Electron.*, vol. 38, no. 11, pp. 14037–14049, Nov. 2023.

[17] J. Guo, H. Wang, G. Xu, H. Han, and M. Su, "Dual-transformer-based DAB converter with controllable integrated inductances," *IEEE Trans. Power Electron.*, vol. 39, no. 5, pp. 6376–6390, May 2024.

[18] G. Xu, J. Wang, H. Wang, Y. Liu, D. Liu, and M. Su, "Coupled-inductor-based dual active bridge converter with soft switching capability and low component count," *IEEE J. Emerg. Sel. Topics Power Electron.*, vol. 10, no. 4, pp. 4771–4782, Aug. 2022.

[19] Y.-D. Kim, C.-E. Kim, K.-M. Cho, K.-B. Park, and G.-W. Moon, "ZVS phase shift full bridge converter with separated primary winding," *IEEE Energy Convers. Congr. Expo.*, San Jose, CA, USA, pp. 484–489.

[20] J. Wang et al., "Design of integrated magnetic transformer for high frequency LLC converter," in *Proc. 4th Int. Conf. HVDC*, Xi'an, China, 2020, pp. 986–991.

[21] Y. Liu, H. Wu, J. Zou, Y. Tai, and Z. Ge, "CLL resonant converter with secondary side resonant inductor and integrated magnetics," *IEEE Trans. Power Electron.*, vol. 36, no. 10, pp. 11316–11325, Oct. 2021.

[22] M. Ahmed, A. Nabih, F. Lee, and Q. Li, "Low-loss integrated inductor and transformer structure and application in regulated LLC converter for 48-V bus converter," *IEEE J. Emerg. Sel. Topics Power Electron.*, vol. 8, no. 1, pp. 589–600, Mar. 2020.

[23] Z. Cao et al., "A low loss orthogonal decoupling magnetic integrated structure for dual active bridge converter," *IEEE Trans. Power Electron.*, vol. 37, no. 6, pp. 7013–7027, Jun. 2022.

[24] J. Yang, Y. Xu, X. Wu, and F. Muhammad, "High-density planar integrated magnetics with two-sided merged inductor windings and integrated cores for resonant DC/DC converter," *IEEE J. Emerg. Sel. Topics Power Electron.*, vol. 12, no. 1, pp. 195–207, Feb. 2024.

[25] J. Muhlethaler, J. Kolar, and A. Ecklebe, "A novel approach for 3D air gap reluctance calculations," in *Proc. 8th Int. Conf. Power Electron.- ECCE Asia*, Jeju, Korea (South), 2011, pp. 446–452.

[26] K. Venkatachalam, C. R. Sullivan, T. Abdallah, and H. Tacca, "Accurate prediction of ferrite core loss with nonsinusoidal waveforms using only steinmetz parameters," in *Proc. IEEE Workshop Comput. Power Electron.*, Mayaguez, PR, USA, 2002, pp. 36–41.

[27] J. Mühlethaler, "Modeling and multi-objective optimization of inductive power components," Swiss Federal Instit. Technol. (ETH) Zurich, 2012. [Online]. Available: https://www.ams-publications.ee.ethz.ch/uploads/tx_ethpublications/Diss_Muehlethaler.pdf

Siddhesh Shinde (Graduate Student Member, IEEE) received the B.E. degree in electrical engineering from the University of Mumbai, India, in 2012, and the M.S. degree in power electronics from the University of Central Florida, Orlando, FL, USA, in 2016. He is currently working toward the Ph.D. degree focuses on the design and thermal management of underground power electronics systems with the Delft University of Technology, The Netherlands.

From 2013 to 2014, he worked as a Project Engineer at the Indian Institute of Technology Bombay, contributing to the development of solar and battery based microinverters funded by the Ministry of New and Renewable Energy, India. From 2017 to 2022, he worked as a Power Electronics Engineer with electric vehicle startups, including NIO and Lucid Motors, contributing to the development of automotive power converters. His research interests include integrated magnetic structures and thermal design for high-power-density dc–dc converters in electric vehicle applications.

Gautam Rituraj (Member, IEEE) received the B.Tech. degree in electrical engineering from Uttar Pradesh Technical University, Lucknow, India, in 2012 and the Ph.D. degree in coupling efficiency improvement and power transfer enhancement in wireless power transfer system for electric vehicle charging applications from the Indian Institute of Technology Guwahati, Guwahati, India, in 2021.

From 2021 to 2025, he was a Postdoctoral Researcher with TU Delft, pursuing his research on off-grid EV charging, standalone microgrid design and optimization, hybrid energy storage integration, and electrolyzer systems. He is currently a Technical Staff Member in the ESP lab, DCE&S group, Department of Electrical Sustainable Energy, Delft University of Technology, The Netherlands. His current research interests include off-grid EV charging systems, electrolyzer systems, dc–dc converters, energy storage integration, analysis and design of wireless power transfer systems, coil design and modelling, and developing power electronic circuits for EV charging.

Dr. Rituraj is a recipient of the Gandhian Young Technological Innovation (GYTI) Appreciation 2021 for his doctoral work and holds one Indian patent. His paper was recognized as a featured article in the *IEEE Open Journal of the Industrial Electronics Society* in 2023.

Gautham Ram Chandra Mouli (Senior Member, IEEE) received the bachelor's and master's in electrical engineering from the National Institute of Technology Trichy, India, and the Delft University of Technology, Delft, The Netherlands, in 2011 and 2013, respectively. He received the Ph.D. degree from the Delft University for the development of a solar-powered V2G electric vehicle charger compatible with CHAdeMO, CCS/COMBO and designed smart charging algorithms (with PRE, ABB and UT Austin), in 2018.

From 2017 to 2019, he was a Postdoctoral Researcher with TU Delft, pursuing his research on power converters for EV charging, smart charging of EVs, trolley busses. He is currently an Associate Professor with the dc systems, Energy Conversion and Storage group in the Department of Electrical Sustainable Energy at the Delft University of Technology, The Netherlands. His current research focuses on electric vehicle charging, PV systems, power electronics and intelligent control.

He was the recipient of the best paper prize in IEEE TRANSACTIONS ON INDUSTRIAL INFORMATICS in 2018, the Best Poster prize at Erasmus Energy Forum 2016, Netherlands and the Best Paper prize at the IEEE INDICON Conference 2009, India, and was awarded the "Most significant innovation in electric vehicles" award from IDtechEx in 2018 and the "Best Tech Idea of 2018" by KIJK for his Ph.D. degree. He is involved in many projects with industrial and academic partners at national and EU level concerning electric mobility and renewable energy such as PV charging of electric vehicles, OSCD, Trolley 2.0, Flexgrid, Flexinet and NEON. He is the coordinator and a Lecturer for the Massive Open Online Course (MOOC) on Electric cars on edX.org with 175 000 learners from 175 countries. He is the Vice-Chair of the IEEE Industrial Electronics Society Benelux chapter.

Vishnu Mahadeva Iyer (Senior Member, IEEE) received the B.Tech. degree in electrical and electronics engineering from the College of Engineering, Trivandrum, KL, India in 2011, the M.E degree in electrical engineering from the Indian Institute of Science (IISc), Bengaluru, KA, India, in 2013, and the Ph.D. degree in electrical engineering from the NC State University, Raleigh, NC, USA, in 2020.

He worked as a Lead Engineer with GE Research, Niskayuna, USA, in 2020 and from 2013 to 2015, as a Power Electronics Engineer with GE Research, Bengaluru, KA, India. In 2020, he joined as an Assistant Professor with the Department of Electrical Engineering, IISc Bengaluru. His research interests include resonant and soft-switched power converters, high-frequency magnetics, control and stability of power electronic converters, and partial power processing.

Pavol Bauer (Senior Member, IEEE) received the master's degree in electrical engineering from the Technical University of Kosice, Slovakia, in 1985, and the Ph.D. degree from Delft University of Technology, in 1995.

He is currently a full Professor with the Department of Electrical Sustainable Energy of Delft University of Technology and head of dc Systems, Energy Conversion and Storage group. He received the title of Professor from the President of Czech Republic at the Brno University of Technology (2008) and Delft University of Technology (2016). He is also honorary Professor with Politehnica University Timisioira in Romania where he got also a honorary doctorate (Dr.h.c). From 2002 to 2003, he was working partially at KEMA (DNV GL, Arnhem) on different projects related to power electronics applications in power systems. He authored or coauthored more than 170 journal and 500 conference papers in his field (with H factor Google scholar 60, Web of Science 40), 8 books, holds 10 international patents and organized several tutorials at the international conferences. He has worked on many projects for industry concerning wind and wave energy, power electronic applications for power systems such as Smarttrafo; HVdc systems, projects for smart cities such as PV charging of electric vehicles, PV and storage integration, contactless charging; and he participated in several Leonardo da Vinci, H2020 and Electric Mobility Europe EU projects as project partner (ELINA, INETELE, E-Pragmatic, Micact, Trolly 2.0, OSCD, P2P, Progressus, Tulip, Flow) and coordinator (PEMCWebLab.com-Edipe, SustEner, Eranet DCMICRO). His main research interests include power electronics for charging of electric vehicles and dc grids.

Dr. Bauer is a Former Chairperson of Benelux IEEE Joint Industry Applications Society, Power Electronics and Power Engineering Society chapter, Chairperson of the Power Electronics and Motion Control (PEMC) council, Chairperson of Benelux IEEE Industrial Electronics chapter, member of the Executive Committee of European Power Electronics Association (EPE), and also Member of international steering committee at numerous conferences.